

NICMOS OBSERVATIONS OF THE TRANSITING HOT JUPITER XO-1b

CHRISTOPHER J. BURKE¹, P. R. MCCULLOUGH², L. E. BERGERON², DOUGLAS LONG², RONALD L. GILLILAND²,
 EDMUND P. NELAN², CHRISTOPHER M. JOHNS-KRULL³, JEFF A. VALENTI², KENNETH A. JANES⁴

(Received April 29, 2010)

Submitted to the Astrophysical Journal

ABSTRACT

We refine the physical parameters of the transiting hot Jupiter planet XO-1b and its stellar host XO-1 using HST NICMOS observations. XO-1b has a radius $R_p = 1.21 \pm 0.03 R_J$, and XO-1 has a radius $R_* = 0.94 \pm 0.02 R_\odot$, where the uncertainty in the mass of XO-1 dominates the uncertainty of R_p and R_* . There are no significant differences in the XO-1 system properties between these broad-band NIR observations and previous determinations based upon ground-based optical observations. We measure two transit timings from these observations with 9 s and 15 s precision. As a residual to a linear ephemeris model, there is a 2.0σ timing difference between the two HST visits that are separated by 3 transit events (11.8 days). These two transit timings and additional timings from the literature are sufficient to rule out the presence of an Earth mass planet orbiting in 2:1 mean motion resonance coplanar with XO-1b. We identify and correct for poorly understood “gain-like” variations present in NICMOS time series data. This correction reduces the effective noise in time series photometry by a factor of two, for the case of XO-1.

Subject headings: planetary systems – stars: individual (GSC 02041-01657)

1. INTRODUCTION

XO-1b is a transiting hot Jupiter planet orbiting a Solar-type star (McCullough et al. 2006). Subsequently, Holman et al. (2006) refined the parameters of the star, XO-1, and planet, XO-1b, with ground based optical photometry (Torres et al. 2008; Southworth 2008). From a theoretical standpoint XO-1b has the properties of a “normal” extrasolar planet, in the sense that the measured mass, M_p , and radius, R_p , of XO-1b agree with the theoretical expectations after taking into account the stellar insolation, and XO-1b likely does not contain a substantial amounts of heavy elements (Burrows et al. 2007). Spitzer Space Telescope observations with IRAC of XO-1b at secondary eclipse detected the presence of a temperature inversion in the outer layers (1 mbar) of the planetary temperature-pressure (T-P) profile (Machalek et al. 2008). The wavelength dependence of the IRAC measurements provides a valuable constraint on the day-side T-P profile and molecular abundances.

Measuring the absorption depth when the planet transits its stellar host as a function of wavelength, here referred to as transmission spectroscopy, provides additional constraints on the planet’s atmosphere. The change in transit depth results from opacity variations as a function of wavelength in the planet’s atmosphere and probes the T-P profile in the outermost (< 1 mbar) layers of the planet’s atmosphere at the terminator (Fortney et al. 2010). To extend transit observations of

XO-1b to the NIR, we present high cadence HST NICMOS observations of XO-1b. The observations were obtained with the G141 grism, which covers the strong absorption features due to H₂O, CO₂, and CH₄. In this work, we present new constraints on the XO-1 system by summing the flux over the entire grism spectrum. The NICMOS broad-band time series provide a precise measurement of R_p , stellar density, ρ_* , and transit timings for which to compare to previous determinations in the optical. Tinetti et al. (2010) present a complementary study to this one using the same NICMOS observations as analyzed here by enhancing the wavelength resolution at the sacrifice of signal to noise. Tinetti et al. (2010) examine the relative change in transit depth across the G141 grism, and they detect the presence of H₂O in the atmosphere of XO-1b.

Currently, NICMOS grism observations for 9 transiting extrasolar planets have used $\gtrsim 120$ HST orbits. Previous analyses of grism broad-band time series with NICMOS have been limited to a factor of 2-3 times worse than the Poisson expectation (HD 209458b - Gilliland & Arribas (2003), Swain et al. (2009); GJ 436b - Pont et al. (2009); HD 149026b Carter et al. (2009)). In this work, we identify and correct for systematics that improve the relative flux precision for broad-band time series to the expected level. The technical details of this work will augment the substantial archival NICMOS grism observations and future NICMOS grism observations of transiting extrasolar planets.

The NICMOS observations are described in § 2. The technical details of the data analysis, improvements in the treatment of systematics for NICMOS grism observations, and a discussion of the expected photometric noise level are given in § 3. The XO-1 system properties are discussed in § 4, and we discuss the results in § 5.

2. OBSERVATIONS

cburke@cfa.harvard.edu

¹ Harvard-Smithsonian Center for Astrophysics, 60 Garden St., Cambridge, MA 02138

² Space Telescope Science Institute, 3700 San Martin Dr., Baltimore, MD 21218

³ Dept. of Physics and Astronomy, Rice University, 6100 Main Street, MS-108, Houston, TX 77005

⁴ Boston University, Astronomy Dept., 725 Commonwealth Ave., Boston, MA 02215

The NICMOS grism observations were designed to gather high cadence time series of the bright, $V=11.2$, star XO-1 during transits of the planet XO-1b (HST program 10998). Gaps in the time series due to Earth occultation necessitate piecing together observations from more than one transit. HST observed a transit event on Feb. 10, 2008 UT (2454506.6 JD) and again three transits later on Feb. 21, 2008 UT (2454518.4 JD). Each visit consists of five HST orbits.

The first-order spectrum of XO-1 from the G141 grism ($1.1 \leq \lambda \leq 1.9 \mu\text{m}$) is positioned on the lower left quadrant (quad 1) of the NIC3 NICMOS detector, and it does not cross any amplifier boundaries (see Figure 1). The zeroth-order spectrum lies on the lower right quadrant (quad 2), and it enables accurate tracking of the spectrum's position. No other stars contribute significant flux in the NIC3 field of view. The Pupil Alignment Mechanism was set at -0.53 mm to defocus the Point Spread Function (PSF). Defocusing spreads the light over more pixels which improves operational efficiency by delaying saturation and improves precision by averaging nonuniform pixel response (Xu & Mobasher 2003). The detector is read out in MULTIACCUM mode with the STEP8 sequence and NSAMP=11, resulting in an overall exposure time 39.953 s for a single MULTIACCUM exposure. Including overheads, the exposure cadence is 49 s between MULTIACCUM exposures. There are ~ 57 exposures per HST orbit. A single direct image in the F166N filter at the beginning of each HST visit provides the reference position of the target for determining the wavelength calibration.

We reduced the data using both custom procedures and publicly-available procedures written in IDL. The reduction begins from the raw science file (`_raw`) rather than the calibrated science file (`_cal`). In summary, the procedure for reducing an image consists of starting from the last-read minus zeroth-read image of a MULTIACCUM image, applying a wavelength dependent flat field, and then correcting bad pixels through bicubic spline interpolation. These data reduction steps are described next, and the resulting images are used to perform broad-band photometry in § 3.

To determine the wavelength dependent flat field and to correct for systematic trends in the photometric time series (see § 3), we map the position of the spectrum on the detector. To measure the spectrum location, we fit a Gaussian to calculate the centroid of the spatial profile for 5 pixel intervals along the dispersion axis. A linear fit to the centroids versus position along the dispersion axis yields the slope of the spectrum on the detector. The lower left panel in Figures 2 & 3 show the spectrum slope as a function of image number within an orbit for the first and second visit, respectively. Each color represents an orbit, and the color code to identify an orbit is given in the lower right panel of the figure. The spectrum slope variation within an orbit is much smaller than the change between orbits. We measure relative shifts in x and y pixel coordinates of the spectrum by cross correlation of the zeroth-order spectrum with respect to a reference image (11-th image in the second orbit of the first visit). The zeroth-order position shifts are projected to the first-order spectrum's dispersion relation position. The projection, $\delta x = -\Delta \cos \alpha$ and $\delta y = -\Delta \sin \alpha$, takes into account the spectrum slope, α , and the pixel dis-

tance between the zeroth-order light and dispersion relation's reference position, $\Delta = 167.93 \text{ pix}$. The top panels in Figure 2 and Figure 3 show the relative x and y pixel coordinate shifts of the dispersion relation's reference position as a function of the image number within an orbit. The dispersion reference position is repositioned within 0.5 pixel between visits and typically 0.2 pixel within a visit.

We follow the procedure outlined in Gilliland & Arribas (2003) to determine the wavelength dependent flat field, and the wavelength of each pixel is determined using the dispersion relation given in Pirzkal et al. (2009). The centroid of the direct image taken at the beginning of each visit determines the reference position of the dispersion relation. A flat field is calculated for each image taking into account the reference position shifts and the spectrum slope variations. The individual flat fields are averaged over an orbit, and the resulting orbit averaged flat field is normalized on quad 1 where the first-order spectrum is located. The orbit averaged flat field is applied to all images within that orbit.

We use four methods to identify the dark, warm, and cosmic ray impacted pixels. We begin with the standard bad pixel mask for the NIC3 camera (Sosey 2002). Second, we identify pixels that significantly vary beyond their empirically determined sample standard deviation throughout an orbit. Third, warm pixels ($> 100 \text{ DN}$) in the region for determining the background level are identified for correction. Fourth, pixels that deviate by $> 3\sigma$ from the Poisson and read noise expectation in both forward and backward differences are identified for correction. On average, each image has 177 pixels (1.1%) for correction on quad 1. We replace affected pixels by the value of a bicubic spline fitted to surrounding pixels.

In addition to the spectrum position and slope, we make use of the G141 filter wheel telemetry to correct for systematic trends in the photometric time series. The filter wheel telemetry indicates that the G141 grism position does not return to the same state in between orbits. The filter wheel telemetry for each visit (Chris Long, private communication) is given as a function of orbit in the lower right panel of Figures 2 & 3. There are two preferred telemetry states of the G141 grism (~ 0.6 and ~ 0.3 fractional telemetry position), and within each of these telemetry states the telemetry do not exactly repeat but have small variations. In the first visit (Figure 2), the filter wheel telemetry anti-correlates with the spectrum slope; The filter wheel telemetry position of 0.6 (orbits 1 & 3) correspond to low spectrum slope, and the filter wheel telemetry position of 0.3 (orbits 2, 4, & 5) corresponds to the higher spectrum slope. In the second visit, the correspondence of filter wheel telemetry and spectrum slope is not as clear.

3. BROAD-BAND LIGHT CURVE ANALYSIS

This section describes the process to extract the broad-band photometric signal from the calibrated images by summing the source flux over the entire first-order spectrum. We describe newly identified systematics of the NIC3 camera and the procedure we follow to simultaneously correct the systematics and fit for the transiting planet model. The result is an improved estimate for the physical properties of the planet XO-1b and star the

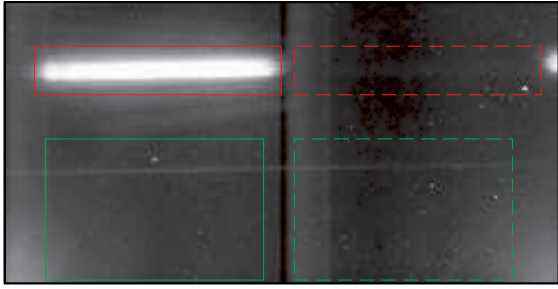


FIG. 1.— Lower two quadrants of the NIC3 camera showing the photometric and background apertures for the target *solid* and blank *dashed* region, left and right respectively. The image is based upon averaging all images in a single orbit. In addition to the first-order spectrum in the upper left, the zeroth-order spectrum is visible in the upper right. The readout amplifier glow is apparent in the lower corners since we analyze raw data rather than the CALNICA pipeline calibrated images, which have the amplifier glow removed.

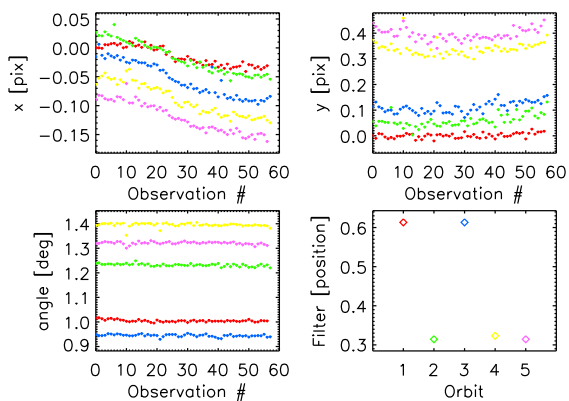


FIG. 2.— *Top Panels:* Evolution of the dispersion relation's reference x and y position throughout the five orbits of the first visit as a function of image number within an orbit. Each color represents an individual orbit as given in the key in the bottom right panel. *Bottom Left:* Spectrum slope as a function of observation number within an orbit. *Bottom Right:* Filter wheel telemetry for each orbit and color key for each orbit within the first visit.

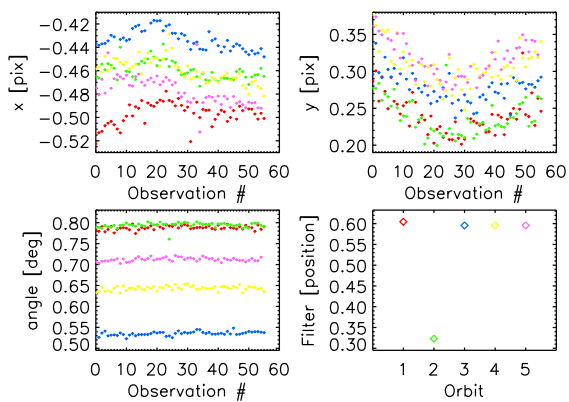


FIG. 3.— Same as Figure 2, but for the second visit.

XO-1.

3.1. Photometry and Expected Noise

We define the source flux to be the sum of counts in a rectangular region enclosing the first-order light minus an estimate of the background flux contribution. The positional shifts of the first-order spectrum (< 1 pix)

are small enough to adopt the same photometric aperture and background region for all visits and orbits. The photometric aperture is a 113×23 pixel region, and the background estimate aperture is 100×65 pixel region located 25 pixels below the photometric aperture. The solid rectangular outlines in Figure 1 illustrate the photometric and background regions, top left and bottom left, respectively. These regions were chosen to minimize flux variations in the extracted photometry after correcting for systematic effects.

The first-order summed flux from XO-1 is shown in Figure 4, where the flux relative to the average out of transit flux is shown phased at the orbital period of XO-1b. Each HST visit is normalized separately. There is a 0.6% relative flux difference between the two HST visits and smaller, but significant 0.2% relative flux differences between orbits within the same visit. The upper left panel of Figure 7 shows in detail the in-transit orbit closest to orbital phase, $\phi = 0.0$. For those data, the empirical rms noise is $\sigma = 555$ ppm per exposure. The expected noise from Poisson noise alone is $\sigma_{\text{poi}} = 180$ ppm per exposure. An additional source of noise arises due to the systematic uncertainty in determining the background level and read noise. To empirically determine the contribution of read noise and background level subtraction to the photometric precision, we perform the aperture photometry on a blank region of quad 2. The target and background regions are the same size as for the first-order spectrum photometry as illustrated by the dashed line regions in Figure 1. The expected noise in the blank region photometry taking into account the Poisson noise, read noise, and the number of pixels in the background and photometry regions is 2300 e^- rms. We measure 5400 e^- rms per exposure variation in the blank region photometry, indicating the presence of non-Gaussian noise in the background. The empirically determined read noise and systematic uncertainty in the determining the background level contributes $\sigma_{\text{back}} = 170$ ppm noise relative to the $3.1 \times 10^7 \text{ e}^-$ counts from XO-1 per exposure. Adding σ_{back} in quadrature with σ_{poi} results in the expected relative noise for photometry of $\sigma_{\text{tot}} = 250$ ppm per exposure. The expected noise is 2.2 times smaller than the empirically determined noise within an orbit. In addition to the higher than expected noise, the residuals qualitatively are distributed uniformly between limits and are non-Gaussian in appearance. This broadened distribution of residuals has been noted previously (see Figure 3 of Carter et al. 2009).

3.2. Correcting for Gain-like Variations

The non-Gaussian residuals in the photometric time series correlate with 7 preferred states imparted by the detector electronics that result in gain-like variations. The 7 states originate from the detector's switching low voltage power supply, which has its clock set to a frequency 7 times lower than the master clock of the timing pattern generator (Bergeron, in preparation). The 7 states were first identified as additional noise in the detector temperature estimates from the bias level (Pirzkal et al. 2009). In this study, we show that the 7 states also impact photometric time series with NICMOS. Which of the 7 states an exposure belongs to is measurable from the zeroth-read image of a MULTIACCUM image. The zeroth-read image is obtained immediately following a re-

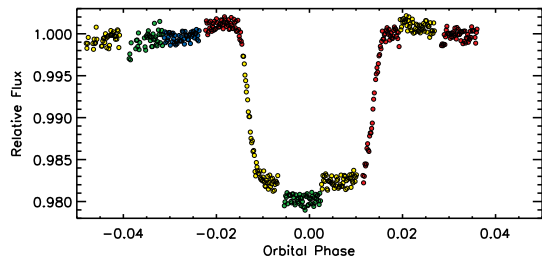


FIG. 4.— Raw relative observed counts for XO-1 phased at the XO-1b orbital period. Data is shown from the first HST visit (*green & red points*) and the second HST visit (*yellow & blue points*). Within a visit, orbits that share the same color share the same filter wheel position.

set of the detector array and it represents the bias level of the MULTIACCUM image. For a more accurate measure of the relative bias level, the zeroth-read image from the first image within an orbit is subtracted, removing any bias structure and faint signal of the spectrum recorded since the array reset. The mean zeroth-read bias level of quad 1 versus the mean zeroth-read bias level of quad 2 for images within an orbit is shown in the upper right panel of Figure 7. The images in this plane form 7 distinct groups. The lower left panel of Figure 7 shows the same relative photometry as in the panel above it, but the measurements that share the same readout state are connected by a line. The color coding is the same as in the upper right panel of Figure 7, where the 7 states are identified. Measurements in the same state systematically over or underestimate the relative flux. We correct for the 7 state effect by removing the average relative flux offset of the state from the relative flux offset averaged over all measurements in an orbit. The result of 7 state correction is shown in the lower right panel of Figure 7. The rms of the residuals is reduced from 550 ppm (before) to 288 ppm (after), a factor of 1.9 improvement. To properly account for the 7 states during times when the flux level is varying rapidly (i.e., during ingress and egress), the 7 state correction is determined after removing the transit model (see below).

3.3. Model Fit to Data

The remaining flux time series, F_{obs} , are fit to the following model,

$$F_{mod} = F_o \times \Psi \times \Phi(P, T_o, M_\star, R_\star, \delta, \tau_{I-IV}, t_1, t_2, u_1, u_2), \quad (1)$$

where $F_o \times \Psi$ is the correction for the observed flux variability due to instrumental effects and intrinsic stellar variability between visits (see below) and Φ represents the relative flux variation due to the transiting planet. The orbital period, $P = 3.941502$ d (Gary, B., private communication), and ephemeris transit midpoint, $T_o = 2453887.74679$ (HJD; Holman et al. 2006), are held fixed, but each visit is allowed to have its own transit midpoint offset (t_1 & t_2) from the fixed ephemeris. This initial ephemeris is based upon a compilation of professional and amateur observations of XO-1. The longer time baseline provided by including amateur observa-

tions allowed a more precise estimate of the ephemeris than previously published ephemerides. We adopt a quadratic limb darkened (u_1 & u_2) transit model as given by Mandel & Agol (2002), and use a Gaussian prior on the stellar mass, $M_\star = 1.027 \pm 0.06 M_\odot$ (Torres et al. 2008). The remaining parameters in Φ are stellar radius, R_\star , planet radius to stellar radius ratio, $\delta = R_p/R_\star$, and first-to-fourth contact transit duration, τ_{I-IV} . From the constraints placed by radial velocity measurements of the XO-1b orbit (McCullough et al. 2006), we assume zero eccentricity. The parameter estimates and their uncertainty are determined following the MCMC procedure outlined in Burke et al. (2007). The prior adopted for R_\star , δ , and τ_{I-IV} results in a uniform prior on R_\star , R_p , and orbital inclination (Burke et al. 2007). The priors for the other parameters are uniform with upper and lower limits well beyond values constrained by the data. The exception to this is limb darkening parameters, which are physically constrained as described in Burke et al. (2007). In particular, we require that the highest surface brightness be located at the center of the disk (i.e., $u_1 \geq 0$). This is consistent with theoretical H-band limb darkening parameters ($u_1 = 0.016$ & $u_2 = 0.441$) for XO-1 (Claret 2000). The time for each observation is taken as the midpoint of the exposure, and is determined from the average of the EXPSTART and EXPEND header keywords. The resulting modified Julian date is converted to barycentric Julian date (BJD) on the Terrestrial Time system (TT) using the barycen IDL routine⁵ (Eastman et al. 2010). The calculated BJD times are ~ 1.3 s earlier than heliocentric Julian date times.

The first orbit of a visit exhibits a systematic ramp up in counts over most of the orbit, which likely results from telescope or instrument settling (Gilliland & Arribas 2003). Subsequent orbits within a visit also have a ramp up effect, but the timescale is much shorter with only the first few measurements impacted. To avoid modeling the ramp-up effect, we discard the entire first orbit of a visit and the first four exposures of each orbit.

To decorrelate against external parameters to correct for the remaining correlated measurements, through trial and error, we find that the remaining residuals correlate with the external parameters: the spectrum's dispersion relation positions, x & y , and the spectrum slope α (Figures 2 & 3). Thus,

$$F_o \times \Psi = F_o \times (1 + c_0 + c_1x + c_2x^2 + c_3y + c_4\alpha), \quad (2)$$

where c_0, \dots, c_4 are the free linear decorrelation coefficients and F_o is arbitrary and fixed (to avoid the degeneracy with c_0) at the average out-of-transit flux of both visits. We empirically find that a successful correction for correlated measurements using the terms in Equation 2 requires treating data from the two filter wheel states separately (see § 2 for a discussion of the filter wheel states). In Figure 4, the green and red points represent data obtained in the first HST visit, and the yellow and blue points represent data obtained in the the second HST visit. In each visit, the orbits are assigned to the two preferred states of the filter wheel positioning (see lower right panel of Figure 2 & 3). Each visit and filter wheel

⁵ <http://astro.uni-tuebingen.de/software/idl/aitlib/astro/barycen.html> ; Input ephemeris file from <http://www.physics.wisc.edu/~craigm/idl/down/JPLEPH.405>

state has its own set of external parameter decorrelation coefficients, c_0, \dots, c_4 . Thus, in Figure 4, the orbits that share a color share the same decorrelation coefficients, however as noted previously, the first orbit for each visit is not included in the MCMC analysis.

There are 5 decorrelation coefficients for each of the 4 visit/filter wheel combinations, resulting in 20 free parameters in Ψ . Including the 8 free parameters specifying the physical parameters of the system, the overall model has a total of 28 free parameters. Before calculating the likelihood of a model for a given set of 28 parameters, the correction for the 7 readout states is applied. The 7 readout states are determined for each orbit independently from the residuals of the model, $F_{obs} - F_{mod}$. The 7 state correction removes the average flux residual for each state with respect to the average residual across all measurements within an orbit. Thus, the 7 state correction does not change the overall flux level of an orbit. The likelihood is modeled as independent Gaussian residuals with uncertainty, $\sigma = 250$ ppm.

The parameters and their uncertainties are based upon an overall MCMC chain of 10^6 steps after a burn-in period. The scale of the proposal steps in each parameter are set using an automated iterative algorithm of proposal step size adjustments until the acceptance fraction, $0.2 < f < 0.3$, is reached. After an initial burn-in period to determine the proposal steps, the proposal distributions are finalized, and the results are based upon the remaining steps. The longest auto correlation length amongst the parameters is 600 steps. Initial tests with a parallel tempering (PT) MCMC algorithm (Gregory 2005a) with 7 parallel chains, did not show any evidence for multimodality amongst the 28 free parameters. Thus, the more time-consuming PT MCMC was not needed to explore the parameter space and helps verify that the single chain reliably explored the parameter space.

4. RESULTS

The resulting transit light curve, residuals, and corrections are shown in Figure 8. The top panel shows F_{obs}/Ψ , the relative flux of the observations after dividing out the best fit (in a χ^2 sense) decorrelation function with correction for the 7 states. The color coding of the points is the same as in Figure 4. The middle panel of Figure 8 shows the residual relative flux of the observations from the complete model. The resulting rms residual, $\sigma_{rms} = 240$ ppm, is slightly less than the expected uncertainty, $\sigma_{tot} = 250$ ppm (see § 3). We presume the latter results from a slight overestimate in the contribution of σ_{back} to σ_{tot} . The lower panel of Figure 8 shows the relative flux correction due to Ψ . The peak to trough relative flux variation in Ψ reaches 0.16% for orbits within the same visit and filter wheel position. For display purposes, Ψ is normalized to its average value for each visit/filter wheel combination. Within a visit, the external parameter decorrelation normalization, c_0 , varies by 0.12% in relative flux. In the 12 days between the two visits, the observed flux of XO-1 varied by 0.6% due to intrinsic variability of the star or the instrument, but we cannot distinguish between these two possibilities from these data. The minimum $\chi^2 = 362.8$ with 362 degrees of freedom indicates the model is an acceptable fit to the data.

Tables 1 & 2 show the resulting parameter estimates

and their uncertainty for XO-1b and XO-1 along with previous determinations from the literature, respectively. The parameter estimates come from the median of MCMC samples, and the uncertainties inscribe 68.3% of the MCMC samples. The uncertainties include the impact of the assumed prior on $M_\star = 1.027 \pm 0.06$. This affects the physical properties of the system that are not directly constrained by the light curve (e.g., R_\star & R_p).

4.1. Light Curve Quality

The light curve quality is high enough that the uncertainty in R_\star and R_p is dominated by the uncertainty in M_\star . A solution assuming fixed M_\star results in $\sigma_\star = 0.008 R_\odot$ and $\sigma_p = 0.013 R_J$ uncertainty in R_\star and R_p , respectively. Table 3 illustrates the sensitivity of the parameters that are directly constrained by the light curve (i.e., independent of M_\star) to fixing the limb darkening parameters at their theoretical expectation. We adopt the H-band values ($u_1 = 0.016$ & $u_2 = 0.441$) from Claret (2000). Fixing the limb darkening parameters results in a $\Delta\chi^2 = 1.3$ worse fit, a non-significant difference in the quality of fit. However, the estimate for R_p/R_\star is 1σ smaller and the uncertainty is 40% smaller. Fixing the limb darkening parameters can lead to more precise model fits, but in the case of high quality data, it may result in lower accuracy when the stellar brightness profile differs from the theoretical expectation (Southworth 2008; Claret 2009). Also shown in Table 3 is the precision possible if the observations were free from systematics. The results were obtained by fixing the decorrelation coefficients, c_0, \dots, c_4 , at the values that minimize χ^2 . The need to correct for systematics reduces the precision in R_p/R_\star by a factor of 5 and reduces the precision in the transit midpoint by a factor of 1.2.

The results shown in Table 3 emphasize the difficulty in judging the light curve quality based upon comparing the resulting uncertainty in the model parameter estimates alone. Assuming a more precise estimate of M_\star (or equivalently R_\star), fixing the limb darkening parameters, or assuming fixed decorrelation coefficients for in-transit data based upon their solution from out-of-transit data, will all result in higher precision for the system parameters, but such procedures may result in less accuracy. Comparing the quality of light curves should not be done out of context. For example, with comparable quality data, the precision for a transit model analysis using fixed limb darkening coefficients should not be directly compared to the precision that results from a transit modeling analysis that allows the limb darkening coefficients to vary.

4.2. Understanding NICMOS Systematics

Recently, Tinetti et al. (2010) analyzed the same observations of XO-1 to measure the transmission spectrum of the atmosphere of XO-1b. Although their analysis focused on individual spectral channels across the G141 grism, their independent analysis techniques share some similarities with the approach adopted in this study. The 7 state correction described in this study is closely related to their correction for “channel-to-channel” correlations (Swain et al. 2008). The gain-like variations associated with the 7 states, which appear to be wavelength independent, would coherently affect the relative flux residuals averaged over all wave-

length channels, and be removed through the “channel-to-channel” corrections. The “channel-to-channel” correction of Swain et al. (2008) cannot be applied to the broad-band photometry, since by definition the broad-band photometry has a single channel. The study by Tinetti et al. (2010) analyzed only the second HST visit to XO-1 (yellow and blue points in Figure 4), as the first visit (green and red points in Figure 4) was deemed too photometrically unstable. By treating orbits in different filter wheel positions separately, we are able to provide reliable model fits (reduced $\chi^2 \sim 1$) using data from both HST visits to constrain the properties of the XO-1 system. Analysis of more NICMOS observations are warranted, but it indicates our methodology enables a coherent procedure to help analyze NICMOS datasets of transiting planets that were previously thought to be too photometrically unstable to provide useful results.

4.3. Impact of Stellar Spots

The light curve analysis assumes the stellar surface is described by the limb darkening function. However, the presence of dark spots or bright faculae on the surface of the star violate this assumption (e.g., Pont et al. 2008). The discovery photometry (0.8% precision) and slow rotation ($v \sin i < 3 \text{ km s}^{-1}$) indicate that XO-1 is not an active star (McCullough et al. 2006). There is a 0.6% apparent flux difference in the measured counts between HST visits; XO-1 appears brighter during visit 2. The photometric stability of the NICMOS cameras is of order $\sim 1\%$ (Thattai et al. 2009), and orbit to orbit differences of 0.2% in flux within a single visit are present. Thus, it is not clear whether the flux difference between the first and second visit is due to intrinsic variability in XO-1 or due to instrumental photometric instability. If the $\eta = 0.006$ decrease in flux results from the appearance of an unocculted dark spot, then the R_p/R_\star as measured for the transit when the dark spot is present needs to be reduced by a factor of $\sqrt{1 - \eta} = 0.997$ to compare to the measured R_p/R_\star when the spot was absent (i.e., the transit depth is deeper when more unocculted dark spots are present). The expected 0.25% change in R_p/R_\star between visits due to the presence of a hypothetical dark spot, is smaller than our precision with which we currently measure R_p/R_\star . To verify this expectation, we added a free parameter to our model allowing each visit to have its own R_p/R_\star . The resulting model negligibly improves the fit, $\Delta\chi^2 < 1$, however $\Delta R_p/R_\star = -0.0003 \pm 0.0009$, or 0.23% lower R_p/R_\star for the second visit. This agrees in size and direction as the expectation, however it is within the statistical uncertainty, and thus we don’t formally adjust the results in Table 1.

4.4. Impact of Correlated Data

The likelihood used in the Bayesian posterior assumes the residuals are independent and can result in underestimated parameter uncertainties if the residuals are not independent (Pont et al. 2006; Carter & Winn 2009). We analyze the sample autocorrelation function (Box et al. 2008) to verify that the correction for systematics removes the temporal correlations present in the raw data, and that our use of the likelihood that assumes independence is valid (Figure 5). To reliably determine the sample autocorrelation especially for large lags, the sam-

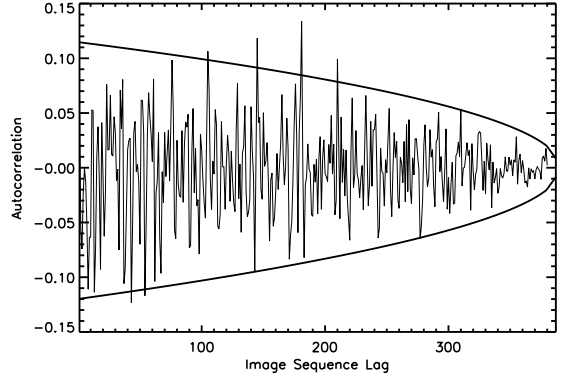


FIG. 5.— Sample autocorrelation of the model fit residuals as a function of image sequence lag. Upper and lower smooth curves indicate the 3σ limits for the null hypothesis that the residuals are independent for the sample autocorrelation statistic.

ple autocorrelation is calculated on the vector of residuals that are ordered by image number rather than time. The smooth upper and lower curves in Figure 5 shows the 3σ limits as to the expectation of the sample autocorrelation statistic if the underlying population of residuals are independent (Kan & Wang 2010). The sample autocorrelation quickly dies off by lag 1, $a_1 = -0.067$, but a few of the lags spike above the 3σ expectation.

We further explore the assumption of independence in the likelihood through Monte Carlo simulation of the raw data and subsequent retrieval of the system parameters. We generate a red noise vector that has the same variance and autocorrelation function as the model residuals. To ensure the sample autocorrelation function does not underestimate the true autocorrelation function, the simulated red noise has an autocorrelation for all lags (≥ 1) 1.5 times the sample autocorrelation shown in Figure 5. In addition to the transit model with red noise, we add correlations with external parameters and 7 state offsets. By comparing the scatter of parameter estimates derived from a χ^2 minimization of the simulated light curves and compare to the uncertainty estimates of an MCMC analysis of the actual data for fixed stellar mass, we find the uncertainties agree within 5% for all the transit model parameters except for the uncertainty in R_\star , which is 18% larger. However, the larger uncertainty in R_\star is negligible compared to the much larger uncertainty in R_\star that results from the uncertainty in M_\star . These tests show that the use of a likelihood assuming independence does not result in a significant underestimate in the parameter uncertainties.

4.5. Transit Timing Variations

The exposure timing information in the NICMOS image headers is on a UTC system, which includes leap seconds. To place timings on a system free of leap seconds, we provide the transit timing measurements from this study along with previous transit timing measurements from the literature on the uniform Barycentric Julian Date Terrestrial Time (TT) system in Table 4. To refine the ephemeris of XO-1b, we analyze precise transit timing measurements from the refereed literature based upon a complete transit and not impacted by strong trends. A subset of the transit timing measurements from Holman et al. (2006) and Cáceres et al. (2009) meet

these characteristics. Specifically, the first 6 transit timing measurements listed in Table 4 are included. The resulting ephemeris is given in Table 1, and the timing residuals from the linear ephemeris model are shown in the top panel of Figure 6. With the published uncertainties on the transit timing measurements, the linear ephemeris model is a moderately poor fit to the transit times. The resulting $\chi^2 = 16.08$ with $\nu = 4$ degrees of freedom has a 2.98σ chance of occurring randomly. A second set of uncertainties for the ephemeris of XO-1b is given in Table 1 that result from scaling the published transit time uncertainties to enforce a reduced $\chi^2 = 1$ for a linear ephemeris. The significance of rejecting the linear ephemeris depends most on transit event 86 in Figure 6. Without transit event 86, the linear ephemeris fit improves to $\chi^2 = 6.94$ with $\nu = 3$, which has a 1.79σ of chance occurrence indicating an acceptable fit.

Additional transit timing measurements of XO-1b, with lower precision, are consistent with the linear ephemeris determined from the higher precision transit timings. We select additional transit timing measurements of XO-1b from the Exoplanet Transit Database (Poddaný et al. 2010) and the Amateur Exoplanet Archive (AXA)⁶ that have observations based upon $>$ half of the transit and not impacted by strong trends. We list the additional transit timings that satisfy these characteristics in Table 4. The transit timings are converted to the BJD (TT) timing system, and we also include the measurement from Raetz et al. (2009). The bottom panel in Figure 6 shows the residual timings (Black points) from the linear ephemeris model, which was determined from the higher quality transit timings (Red points). These additional transit timings have a $\chi^2 = 23.2$ for $\nu = 23$ indicating the linear ephemeris model is adequate for these data.

The transit timing residuals from a linear ephemeris shown in Figure 6 qualitatively give the appearance for a sinusoidal pattern (Gary, B., private communication). Adding a long period sinusoidal component to a linear ephemeris results in a $\Delta\chi^2 = 11.6$ improvement from the linear ephemeris, with a period for the sinusoidal component of 118.3 transit cycles (463 day). Bayesian evidence is one method to quantify the most probable model that describes the data. The details to calculate the Bayesian odds ratio between a linear ephemeris model and the linear+sinusoid ephemeris is given in Appendix A. Using the transit timing measurements in Table 4, the odds ratio of the linear+sinusoidal model to linear model is 5:1. This is substantial evidence in favor of the linear+sinusoidal model, but much less than the 100:1 odds ratio typically accepted as a decisive result.

Overall, the linear+sinusoidal model cannot be distinguished from the linear model, and given the current data both models are acceptable descriptions of the data. The most likely value for $P_{\text{sin}} = 6.84$ transit events (26.77 day), with the previously identified longer period $P_{\text{sin}} = 120$ transit events (470 day), the second most likely solution. The preference for a linear+sinusoid model is weakened, odds ratio 2:1, when the transit timing measurement from the top panel of Figure 6 that most significantly departs from the linear ephemeris is

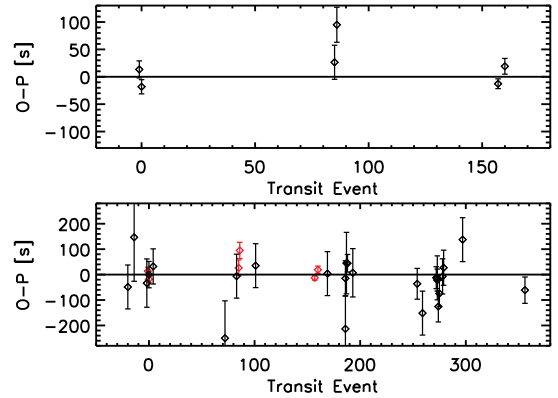


FIG. 6.— *Top*: Deviations of high precision transit timings of XO-1b from the literature and new timings from this work from a linear ephemeris model. From left to right, measurements with KeplerCam on the FLWO 1.2m (Holman et al. 2006), SOFI on the NTT and ISAAC on UT1 (Cáceres et al. 2009), and results from the two HST visits reported in this work. The ephemeris of XO-1b is calculated from these transit timings. *Bottom*: Deviations of additional transit timing measurements of XO-1b from the ephemeris derived in this work (black points). The timing residuals from the top panel are reproduced in this panel (red points).

not included in the analysis.

One potential source of Transit Timing Variations (TTV) is the dynamical influence of additional planets orbiting XO-1 (Holman & Murray 2005; Agol et al. 2005). In particular, the amplitude of TTV for Earth mass planets orbiting at the 2:1 interior or exterior mean-motion resonance with a hot Jupiter planet like XO-1b can reach >50 s (Haghighipour et al. 2009). A full analysis on the limits for companions to XO-1b from the null detection of TTV for XO-1b is beyond the scope of this work (Agol et al. 2005; Agol & Steffen 2007). However, we use the Bayesian evidence calculation to rule out the presence of Earth mass planets in an exterior 2:1 mean motion resonance with XO-1b. We model the TTV of XO-1b due to a coplanar companion at the exterior 2:1 mean motion resonance by adding a sinusoid with an expected period of $72.2P$ (Agol et al. 2005) to the transit timing measurements in Table 4. Amplitudes >45 s for the sinusoid TTV result in an odds ratio $>100:1$ for a decisive detection.

5. DISCUSSION & CONCLUSION

Without the interference of the Earth's atmosphere, space based observations provide an opportunity to achieve high precision, Poisson-limited photometric observations. However, the thermal forcing from the orbital cycle of HST and uncorrected instrumental systematics present a challenge to Poisson limited performance. We correct for gain-like variations in high cadence, high precision time series observations in NICMOS, which improve by a factor of two the relative flux measurement. Although the baseline of observations is limited, there is some evidence that the non-repeatability in the G141 grism positioning between orbits affects the system throughput at the 0.12% level in relative flux. When observations taken with similar grism positioning are grouped together, only a few terms related to the PSF positioning and shape are needed to decorrelate the systematics that appear on the HST orbital time scale. The remaining source of noise is consistent with Poisson and the uncertainty in determining the background level.

⁶ <http://brucegary.net/AXA/x.htm>

Despite the improved modeling of the systematics, the physical transiting planet model contains some degeneracy with the corrections for systematics. The largest impact is for determining the transit depth, R_p/R_* , which has an uncertainty 5 times larger than if the observations were of equivalent quality but free from red-noise systematics. Parameters such as a/R_* and transit timing are less sensitive to the treatment of red-noise systematics. Southworth (2008) reaches similar conclusions for the analysis of the high quality light curves of HD 209458b taken with the STIS on HST (Brown et al. 2001; Knutson et al. 2007). This emphasizes the necessity of simultaneous fitting of the transit model and systematics in order to provide a more realistic assessment of the uncertainties.

Despite the limitations from needing to correct for the systematics, we greatly improve upon the precision for determining the properties of XO-1b directly measurable from the light curve such as a/R_* , R_p/R_* , ρ_* , and transit timing. We find no significant difference in the determination of R_p/R_* between the NIR and previous determinations in the optical (Torres et al. 2008; Southworth 2008, Reproduced in Tables 1 & 2). Using the same data set as this study, Tinetti et al. (2010) independently find a similar absorption depth averaged over the full wavelength coverage. Using transmission spectroscopy, precise and accurate measurements of the transit depth as a function of wavelength are sensitive to opacity variations in the upper levels (1 mbar) of the planetary atmosphere, and theoretical planetary atmosphere models can be used to interpret these measurements to constrain the abundance of molecules and temperature-pressure profiles (Seager & Sasselov 2000; Brown 2001; Madhusudhan & Seager 2009; Fortney et al. 2010). For example, in their analysis of G141 grism data for HD 149026b, Carter et al. (2009) find a larger absorption depth averaged over the G141 grism when compared to optical and Mid-IR measurements than the theoretical models predict. The technical improvements to NICMOS data analysis that we outline in this study may lead to a more precise estimate of the absorption depth in the large archive of NICMOS grism observations of transiting extrasolar planets.

The transit light curve alone does not allow measuring R_p , and with the quality of light curve from this work, the uncertainty in R_p is dominated by the adopted estimate for M_* based upon stellar isochrones (Torres et al. 2008). Alternatively, measuring the parallax of XO-1, along with T_{eff} , apparent magnitude, and bolometric correction determinations, yields a constraint on R_* . This constraint on R_* and the transit light curve will provide a separate estimate for M_* . As part of the proposal for these NICMOS observations, Fine Guidance Sensor (FGS) on HST observations were obtained to measure the parallax of XO-1. We estimate the FGS distance will provide an estimate of R_* with an uncertainty of 5%, and this will provide a 15% constraint on M_* using the transit light curve from this study. Asteroseismology provides an additional estimate of ρ_* and has recently been

demonstrated to yield very precise estimates for the stellar host and planet in the case of HD 17156b (Nutzman, in preparation), and will be a routine procedure for the transiting planets found around the brighter stars with the Kepler mission (Gilliland et al. 2010). Measuring the bulk mass and radius of planets with the highest precision will require improvements in understanding the mass and radius of their stellar hosts (Southworth 2008).

The improved precision of the NICMOS time series photometry has provided two additional measurements of the mid-transit time of arrival. The timing between the two HST visits analyzed in this work is different by 2σ from a linear ephemeris. Also, a single transit measurement from (Cáceres et al. 2009) departs most significantly from a linear ephemeris. Based upon the current measurements of XO-1b transit timings, any bona fide TTV for XO-1b will likely have a peak-to-trough amplitude <90 s, and if the TTV are concentrated in single events, then single timing precision needs to be <23 s. The HST observations presented in this study achieved $\sigma=8.6$ s and $\sigma=15$ s precisions in transit timing. The non continuous nature of HST observations negatively impacts the transit timing. The timing precision with HST can be improved by optimizing coverage of the ingress and egress portion of the light curve. However, transit timing measurements with $\sigma=13$ s precision are possible with ground based observations as demonstrated on XO-1b by Holman et al. (2006). More detailed analysis is warranted, but the current transit timing data rule out coplanar Earth mass companions to XO-1b orbiting in 2:1 mean motion resonance. There have been no additional radial velocity measurements published since the discovery paper (McCullough et al. 2006). Additional radial velocity measurements can aid in constraining the presence of additional planets orbiting XO-1.

The Bayesian evidence calculation that we outline in Appendix A can be applied to other transit timing data sets. The simplified modeling of TTV from a linear ephemeris with a sinusoidal component makes the model selection process numerically expedient. As the quantity and quality of transit timing measurements expands from ground-based observations and especially with the contributions of the *CoRoT* and *Kepler* missions (Csizmadia et al. 2010; Gilliland et al. 2010b), early discovery of TTV will aid in prioritizing and planning the followup observations (Ford 2008).

This work benefited from discussions with Philip Nutzman, Dan Fabrycky, Joe Hora, David Charbonneau, and Jeff Stys. We thank Mark Swain and Pieter Dieroo for conversations about spectrophotometry with NICMOS. We thank Josh Winn and Valentin Ivanov for discussing their published transit timings, and the following observers for their generosity in making their transit timing measurements publicly available, Anthony Ayiomamitis, Cindy Foote, Bruce Gary, Joao Gregorio, Bill Norby, Gregor Srdoc, Jaroslav Trnka, and Tonny Vanmunster.

APPENDIX

BAYESIAN EVIDENCE FOR SINUSOIDAL TRANSIT TIMING VARIATIONS

Bayesian evidence is one method to quantify the most probable model that describes the data, and we follow the procedure as outlined in Gregory (2005a,b, 2007); Ford & Gregory (2007) to calculate the Bayesian odds ratio between the linear ephemeris model and the linear+sinusoid ephemeris model. The algorithm presented by Gregory (2005a) is tailored to quantify the odds for a radial velocity data set to be modeled by no planet, one planet, or $>$ one planet, and we independently implement the algorithm for the model comparison problem at hand. We model the transit timing ephemeris as

$$T_o + E \times P_{\text{lin}} + a \sin \left(\frac{2\pi E}{P_{\text{sin}}} + \phi \right), \quad (\text{A1})$$

where the free parameters are the ephemeris zeropoint, T_o , linear ephemeris period, P_{lin} , amplitude of the sinusoidal component, a , sinusoidal component period, P_{sin} , and sinusoidal component phase, ϕ . The independent variable in the model is the transit event, E . Thus, we calculate the odds ratio between the linear ephemeris model with only two free parameters, T_o & P_{lin} , and the full linear+sinusoid model with five free parameters as shown in Equation A1. We employ the independent Gaussian model for the residuals in the likelihood. We include an additional free parameter in the likelihood that scales the reported errors on the transit timing measurements, s . Allowing s to vary enables the odds ratio between the competing models to take into account our incomplete knowledge as to the overall scaling of the transit timing uncertainties. However, we are assuming that the transit timing uncertainties are correct in a relative sense. Ford & Holman (2007) employ the same linear+sinusoid ephemeris model to characterize and simulate the detection of the TTV signature from a Trojan companion using a lomb-scargle periodogram approach.

The priors for T_o and P_{lin} are uniform since they are already well determined, and their prior range accommodates the constraints placed by the data. We adopt a Jeffreys prior for s that is constrained between $0.25 < s < 4.0$. We adopt a modified Jeffreys prior for a with a break at 1.0 s and maximum of 10^4 s. The maximum a is the largest expected amplitude of transit timing variations expected in the planetary regime (Holman & Murray 2005). Based upon the discussion in Gregory (2007), we choose a Jeffreys prior for P_{sin} with a minimum of 0.9 transit events and a maximum of 1000 yr. The prior for $0 < \phi < 2\pi$ is uniform. The PT MCMC algorithm has 7 parallel chains, and an automated iterative algorithm of proposal step size adjustments until the acceptance fraction, $0.2 < f < 0.3$, is reached. The calculation is based upon the MCMC steps after the proposal step sizes are finalized. The linear+sinusoid ephemeris model is not optimized for the complicated signature TTV signals that can be present and will underestimate the importance of a TTV signature that is concentrated in few events. However, a variety of TTV signatures are qualitatively sinusoidal (e.g., Ford & Holman 2007; Haghighipour et al. 2009), and in general, the dynamical variations of the osculating elements in resonant interactions are well described by expansions of oscillating terms (Murray & Dermott 1999).

The Bayesian Information Criterion (BIC) is an approximation to the Bayesian evidence that is most accurate in the limit of a large number of measurements with a simple likelihood surface (Kass & Raftery 1995). In this example, the number of transit timing measurements is small, and the multimodal likelihood surface invalidates the Taylor series expansion approximation implicit in BIC. However, the $\Delta\text{BIC}=5.2$, between the linear and linear+sinusoidal model mildly prefers the linear+sinusoidal model. $\Delta\text{BIC}>10$ is necessary for a decisive decision with the BIC (Kass & Raftery 1995). Both the Bayesian evidence and BIC show that there is a mild preference for the linear+sinusoidal model, but not a definitive one.

REFERENCES

- Agol, E., Steffen, J., Sari, R., & Clarkson, W. 2005, MNRAS, 359, 567
 Agol, E., & Steffen, J. H. 2007, MNRAS, 374, 941
 Box, G. E. P., Jenkins, G. M., & Reinsel, G. C. 2008, Time Series Analysis: Forecasting and Control (4th ed.; Hoboken, N. J.: John Wiley)
 Brown, T. M. 2001, ApJ, 553, 1006
 Brown, T. M., Charbonneau, D., Gilliland, R. L., Noyes, R. W., & Burrows, A. 2001, ApJ, 552, 699
 Burke, C. J., et al. 2007, ApJ, 671, 2115
 Burrows, A., Hubeny, I., Budaj, J., & Hubbard, W. B. 2007, ApJ, 661, 502
 Cáceres, C., Ivanov, V. D., Minniti, D., Naef, D., Melo, C., Mason, E., Selman, F., & Pietrzynski, G. 2009, A&A, 507, 481
 Carter, J. A., & Winn, J. N. 2009, ApJ, 704, 51
 Carter, J. A., Winn, J. N., Gilliland, R., & Holman, M. J. 2009, ApJ, 696, 241
 Claret, A. 2000, A&A, 363, 1081
 Claret, A. 2009, A&A, 506, 1335
 Csizmadia, S., et al. 2010, A&A, 510, A94
 Dahlen, T., Sosey, M., & Bergeron, E. 2009, NICMOS ISR, 2009-003
 Eastman, J., Siverd, R., & Gaudi, B. S. 2010, arXiv:1005.4415
 Ford, E. B., & Gregory, P. C. 2007, Statistical Challenges in Modern Astronomy IV, 371, 189
 Ford, E. B., & Holman, M. J. 2007, ApJ, 664, L51
 Ford, E. B. 2008, AJ, 135, 1008
 Fortney, J. J., Shabram, M., Showman, A. P., Lian, Y., Freedman, R. S., Marley, M. S., & Lewis, N. K. 2010, ApJ, 709, 1396
 Gilliland, R. L. & Arribas, S. 2003, NICMOS ISR, 2003-001
 Gilliland, R. L., et al. 2010, PASP, 122, 131
 Gilliland, R. L., et al. 2010, ApJ, 713, L160
 Gregory, P. C. 2005, ApJ, 631, 1198
 Gregory, P. C. 2005, Bayesian Logical Data Analysis for the Physical Sciences, Cambridge University Press, Cambridge, UK
 Gregory, P. C. 2007, MNRAS, 374, 1321
 Haghighipour, N., Agol, E., Eastman, J. D., Ford, E. B., Gaudi, B. S., Holman, M. J., Steffen, J., & Veras, D. 2009, astro2010: The Astronomy and Astrophysics Decadal Survey, 2010, 109
 Holman, M. J., & Murray, N. W. 2005, Science, 307, 1288
 Holman, M. J., et al. 2006, ApJ, 652, 1715
 Kan, R., & Wang, X. 2010, Journal of Econometrics, 154, 2, 101
 Kass, R. E., & Raftery, A. E. 1995, Journal of the American Statistical Association, 90, 430, 773
 Knutson, H. A., Charbonneau, D., Noyes, R. W., Brown, T. M., & Gilliland, R. L. 2007, ApJ, 655, 564

- Machalek, P., McCullough, P. R., Burke, C. J., Valenti, J. A., Burrows, A., & Hora, J. L. 2008, *ApJ*, 684, 1427
- Madhusudhan, N., & Seager, S. 2009, *ApJ*, 707, 24
- Mandel, K., & Agol, E. 2002, *ApJ*, 580, L171
- McCullough, P. R., et al. 2006, *ApJ*, 648, 1228
- Murray, C. D., & Dermott, S. F. 1999, *Solar system dynamics* by Murray, C. D., 1999
- Pirzkal, N., Bohlin, R., & Thatte, D. 2009, NICMOS ISR, 2009-006
- Pirzkal, N., Grumm, D., Bergeron, E. 2009b, NICMOS ISR, 2009-007
- Poddaný, S., Brát, L., & Pejcha, O. 2010, *New Astronomy*, 15, 297
- Pont, F., Zucker, S., & Queloz, D. 2006, *MNRAS*, 373, 231
- Pont, F., Knutson, H., Gilliland, R. L., Moutou, C., & Charbonneau, D. 2008, *MNRAS*, 385, 109
- Pont, F., Gilliland, R. L., Knutson, H., Holman, M., & Charbonneau, D. 2009, *MNRAS*, 393, L6
- Raetz, S., et al. 2009, *Astronomische Nachrichten*, 330, 475
- Seager, S., & Sasselov, D. D. 2000, *ApJ*, 537, 916
- Sosey, M. 2003, NICMOS ISR, 2002-001
- Southworth, J. 2008, *MNRAS*, 386, 1644
- Southworth, J. 2009, *MNRAS*, 394, 272
- Swain, M. R., Vasisht, G., & Tinetti, G. 2008, *Nature*, 452, 329
- Swain, M. R., et al. 2009, *ApJ*, 704, 1616
- Thatte, D., et al. 2009, NICMOS Data Handbook, version 8.0, (Baltimore, STScI)
- Tinetti, G., Deroo, P., Swain, M. R., Griffith, C. A., Vasisht, G., Brown, L. R., Burke, C., & McCullough, P. 2010, [arXiv:1002.2434](https://arxiv.org/abs/1002.2434)
- Torres, G., Winn, J. N., & Holman, M. J. 2008, *ApJ*, 677, 1324
- Wilson, D. M., et al. 2006, *PASP*, 118, 1245
- Xu, C., & Mobasher, B. 2003, NICMOS ISR, 2003-009
- Yi, S., Demarque, P., Kim, Y.-C., Lee, Y.-W., Ree, C. H., Lejeune, T., & Barnes, S. 2001, *ApJS*, 136, 417

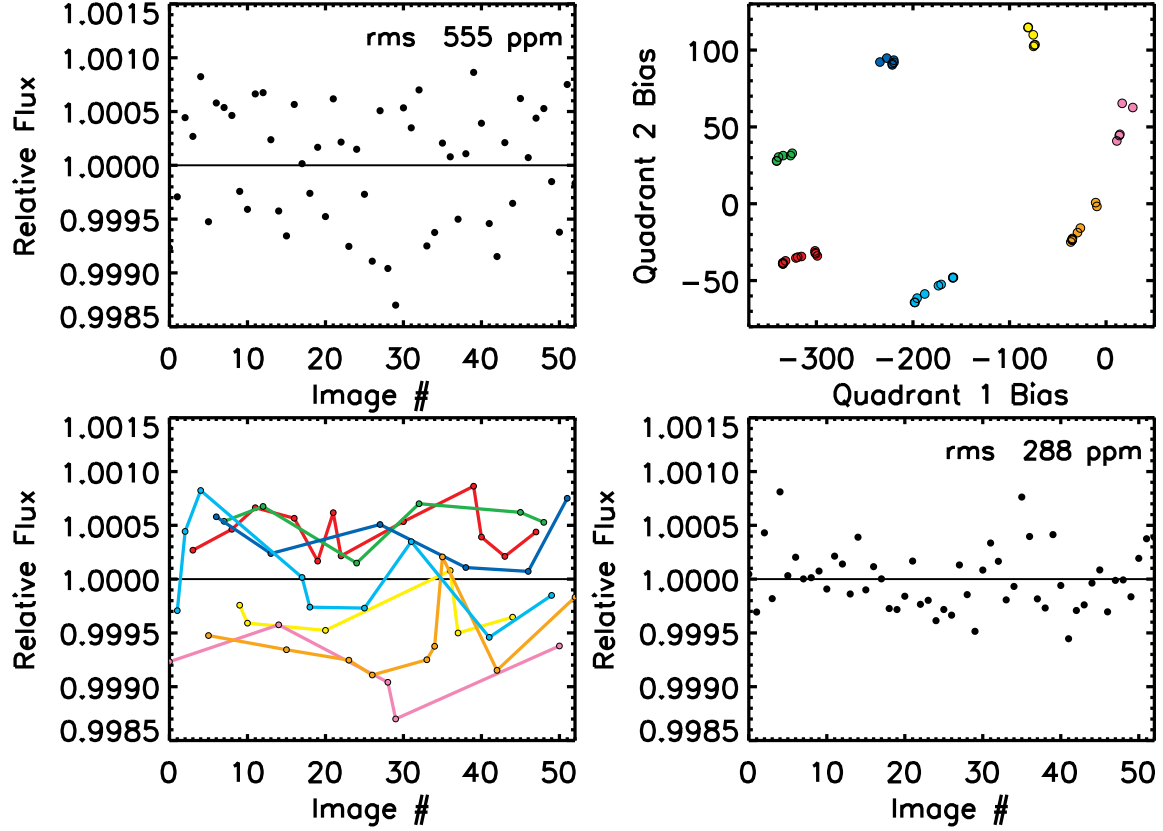


FIG. 7.— *Top Left*: Raw relative flux for the single orbit fully in transit as a function of image number within an orbit. The noise is 2.2 times higher than expected and broadly distributed (i.e., non-Gaussian). *Top Right*: Zeroth-read bias level from the lower left detector quadrant (quad 1) versus the lower right detector quadrant (quad 2) for the same orbit as shown in top left figure. The points are color coded into 7 distinct state groupings. *Lower Left*: The relative flux observations that share the same 7 state groupings are connected by lines with the same color coding as the top right figure. The observations for each state are systematically above or below the mean flux level. *Lower Right*: Each group is forced to the average flux level of an orbit resulting in nearly a factor of 2 improvement in the noise. The remaining correlated red-noise is removed by decorrelation with external parameters.

TABLE 1
Planet Properties - XO-1b

Parameter	This Work	Torres et al. (2008)	Southworth (2008, 2009)
Mass, M_p [M_J]	0.92 ± 0.08	0.92 ± 0.08	0.94 ± 0.07
Radius, R_p [R_J]	1.21 ± 0.03	1.21 ± 0.04	1.22 ± 0.07
Velocity semiamplitude, K [m s^{-1}]	116 ± 9^c
Semimajor axis, a [A.U.]	0.049 ± 0.001	0.0493 ± 0.0009	0.0499 ± 0.0008
Orbital inclination, i [deg]	88.8 ± 0.2	$88.8 \pm_{-0.3}^{+0.7}$	89.1 ± 0.8
Scaled semimajor axis, a/R_*	11.24 ± 0.09	$11.55 \pm_{-0.45}^{+0.03}$...
Planet-to-star radius ratio, R_p/R_*	0.1320 ± 0.0005	0.1326 ± 0.0004	0.1317 ± 0.0019
Transit duration (1 st -4 th contact), τ_{I-IV} [hr]	2.971 ± 0.006
Ingress/Egress duration (1 st -2 nd contact), τ_{I-II} [hr]	0.366 ± 0.007
Impact parameter, b	0.23 ± 0.04	$0.24 \pm_{-0.14}^{+0.04}$...
Planet-to-orbit radius ratio, R_p/a	0.0117 ± 0.00012	...	0.01166 ± 0.00035
Star-to-orbit radius ratio, R_*/a	0.0890 ± 0.0007	...	0.0886 ± 0.0019
Summed radius-to-orbit ratio, $(R_* + R_p)/a$	0.1007 ± 0.0008	...	0.1003 ± 0.0022
Planet gravity, $\log g_p$ [cgs]	3.19 ± 0.03	3.21 ± 0.04	3.199 ± 0.04
Planet density, ρ_p [g cm^{-3}]	0.64 ± 0.05	0.65 ± 0.09	0.69 ± 0.08
Safronov, Θ	0.073 ± 0.006	0.0744 ± 0.006	...
Orbital Period, P [day]	$3.94150685 \pm 0.00000091 \pm 0.0000018^a$		
Time of midtransit, T_o [BJD(TT)]	$2453887.74774 \pm 0.00011 \pm 0.00022^{a,b}$		

^a The second set of uncertainties correspond to enforcing reduced $\chi^2 = 1$ for a linear ephemeris model through scaling the uncertainties in the transit timing measurements.

^b Time is on the BJD Terrestrial Time (TT) system. For times on the BJD (UTC) system subtract 65.184 s.

^c Adopted from McCullough et al. (2006)

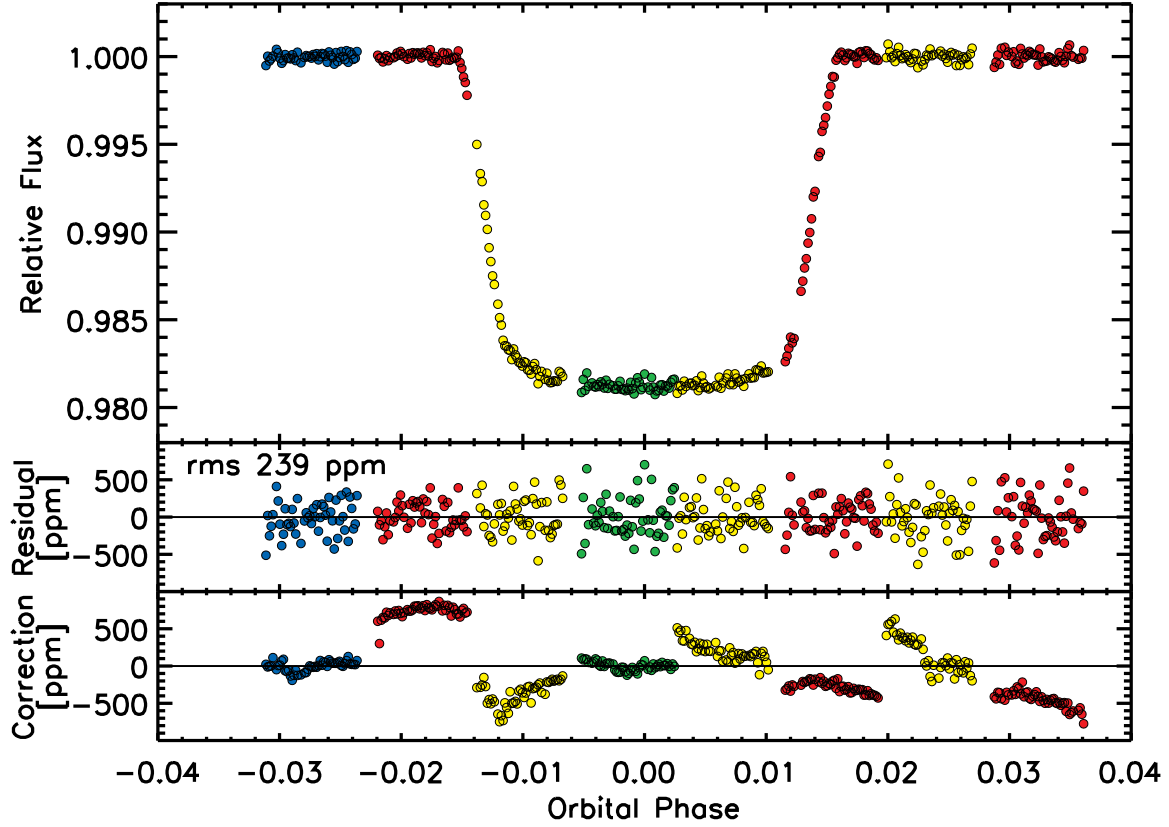


FIG. 8.— *Top*: Best fit relative flux of the observations after correction for the 7 readout states and decorrelation with external parameters. *Middle*: Residual from the best fit transit model and corrections. *Bottom*: Best fit correction for the external parameter decorrelation. The color coding is the same as Figure 4

TABLE 2
Stellar Properties - XO-1

Parameter	This Work	Torres et al. (2008)	Southworth (2009)
Mass, M_{\star} [M_{\odot}]	1.027 ± 0.06^a	...	1.066 ± 0.051
Radius, R_{\star} [R_{\odot}]	0.94 ± 0.02	0.934 ± 0.035	0.95 ± 0.025
Effective temperature, T_{eff} [K]	$5750 \pm 75^{a,b}$
Metallicity [Fe/H]	$0.02 \pm 0.08^{a,b}$
Stellar gravity, $\log g$ [cgs]	4.50 ± 0.01	$4.509 \pm_{-0.027}^{+0.018}$	4.510 ± 0.018
Stellar density, ρ_{\star} [g cm^{-3}]	1.73 ± 0.04	$1.877 \pm_{-0.21}^{+0.015}$	1.75 ± 0.11
First limb darkening coeff., u_1	$< 1\sigma \text{ U.L. } 0.07$
Second limb darkening coeff., u_2	0.35 ± 0.08

^a Adopted from Torres et al. (2008)

^b Adopted from McCullough et al. (2006)

TABLE 3
Precision of Light Curve

Parameter	limb free	limb fixed	Sys fixed
a/R_{\star}	11.24 ± 0.09	11.28 ± 0.09	11.26 ± 0.07
R_p/R_{\star}	0.1320 ± 0.0005	0.1316 ± 0.0003	0.1316 ± 0.0001
τ_{I-IV} [dy]	0.1238 ± 0.0003	0.1240 ± 0.0002	0.1240 ± 0.0002
t_1 [s]	$\sigma=8.6$	$\sigma=8.6$	$\sigma=6.9$

TABLE 4
Transit Timing Measurements

BJDo (TT) ^a	σ [day]	Source
2454506.56417	0.00010	This Work
2454518.38906	0.00017	This Work
2453883.80639	0.00018	Holman et al. (2006)
2453887.74753	0.00015	Holman et al. (2006)
2454222.77613	0.00036	Cáceres et al. (2009)
2454226.71843	0.00037	Cáceres et al. (2009)
2453808.9170	0.0010	AXA ^b ; Poddaný et al. (2010)
2453832.5683	0.0020	"
2453879.8643	0.0011	"
2453887.7477	0.0006	"
2453903.5141	0.0008	"
2454214.8927	0.0010	"
2454285.8403	0.0010	"
2454553.8624	0.0010	"
2454620.8655	0.0015	"
2454620.8678	0.0008	"
2454624.8100	0.0014	"
2454628.7515	0.0004	"
2454648.4586	0.0011	"
2454888.8900	0.0007	"
2454908.5962	0.0010	"
2454959.8375	0.0005	"
2454963.7789	0.0005	"
2454963.7790	0.0010	"
2454967.7192	0.0007	"
2454971.6613	0.0006	"
2454983.4866	0.0008	"
2454987.4285	0.0008	"
2455058.3769	0.0010	"
2455290.9235	0.0006	"
2554171.5333	0.0017	Raetz et al. (2009)

^a NOTE: Times are on the BJD Terrestrial Time (TT) system. For times on the BJD UTC system subtract 65.184 s for times before 2454832.5 Julian Date (UTC) and 66.184 s for times after.

^b Amateur Exoplanet Archive -
<http://brucegary.net/AXA/x.htm>